Rough surface NiFe$_2$O$_4$@Au/Polydopamine with a magnetic field enhanced photothermal antibacterial effect

Yunqi Xu [a], Kang Wang [a], Senlin Zhao [b,c,*], Qingshan Xiong [d], Guanghui Liu [e], Yan Li [a], Qunling Fang [d], Xinglong Gong [a,*], Shouhu Xuan [a,*]

[a] CAS Key Laboratory of Mechanical Behavior and Design of Materials, Department of Modern Mechanics, University of Science and Technology of China, Hefei 230027, PR China
[b] Department of Colorectal Surgery, Fudan University Shanghai Cancer Center, 270 Dong'an Road, Shanghai 200032, PR China
[c] Department of Oncology, Shanghai Medical College, Fudan University, 270 Dong'an Road, Shanghai, 200032, PR China
[d] School of Food and Biological Engineering, Key Laboratory of Metabolism and Regulation for Major Diseases of Anhui Higher Education Institutes, Hefei University of Technology, Hefei 230009, PR China
[e] School of Energy, Materials and Chemical Engineering, Hefei University, 99 Jinxiu Avenue, Hefei, Anhui 230601, PR China

ARTICLE INFO

ABSTRACT

Infectious diseases caused by drug-resistant bacteria bring an increasing threat to public health. Thus, finding an effective approach equipped with a synergistic antibacterial performance becomes a critical challenge. This work reports a NiFe$_2$O$_4$@Au/Polydopamine core/shell nanosphere with rough surface, which exhibits a photothermal and magnetolytic coupling antibacterial behavior. The Au/Polydopamine (Au/PDA) hybrid layer, covered on the stable magnetic NiFe$_2$O$_4$ nanosphere by a one-step polymerization method, possesses an excellent photothermal effect. Simultaneously, the superparamagnetic characteristic offers the NiFe$_2$O$_4$@Au/Polydopamine with fantastic magnetolytic force to the biological organism under a rotating external magnetic field. It is found that the NiFe$_2$O$_4$@Au/PDA core/shell nanospheres show good photothermal antibacterial performance (808 nm laser irradiation) on both *Escherichia coli* and *Staphylococcus aureus*. Notably, the photothermal antibacterial performance can be significantly improved under applying the rotating magnetic field. This novel photothermal-magnetolytic coupled antimicrobial method supplies a high performance photothermal bactericidal therapy *via* a remote conduction and reduces the possible damage to normal tissue caused by overheating. Besides bactericidal therapy, the easily and scalable magnetolytic enhancing method is believed to possess high potential in drug delivery, antitumor, and bioseparation.

1. Introduction

Bacteria are known to be highly adaptable to harsh environments and can proliferate rapidly, while being pathogens of many diseases [1,2]. With the uncontrolled use of antibiotics, multiple drug-resistant superbugs are surviving and spreading widely, which causes serious human infections and insurmountable public health problems worldwide [3,4]. Due to the decreasing effectiveness of conventional antibiotics, it is imperative to find improved strategies to overcome drug-resistant bacteria and biofilm-associated infections [5–7]. Recently, with the fast development of nanotechnology, many novel nanoplatforms treated for terrible diseases have been intensively studied. Fortunately, besides the anti-tumor, these nanobiological methods also provide many new insights into the treatment of drug-resistant superbugs. Among them, the sonodynamic therapy [8], photodynamic therapy [9], photothermal therapy [10–12], magnetolytic therapy [13–15] and a variety of combination therapies [16–18] have been extensively studied and gradually applied in the field of antibacterial [19–23].

Photothermal therapy attracts increasing interest in antibacterial due to its simple processing and remote operation [24]. Under applying light of the appropriate wavelength, the excited photothermal material often leads to a rapid increase in temperature due to the photon-induced lattice vibrations. As a result, the membrane and internal proteins of the cell or bacteria can be destroyed and rendered to be inactive. Among various strategies to fight bacterial infections, photothermal therapy is a promising antibacterial method owing to its low toxicity, high

selectivity, low invasiveness and lack of resistance. During the past decade, various nanoplatforms with excellent photothermal conversion efficiency have been developed to kill cancer cells or bacteria, such as carbon-based nanostructures [25], noble metal nanostructures [26], metal oxides [27], two-dimensional materials [28,29], and polymers [30]. For example, Liu Z. et al. [24] prepared polyvinyl alcohol-coated polypyrrole nanospheres as near-infrared light absorbers for photothermal therapy. Their product showed high performance in cancer ablation therapy. Yang H.H. et al. [31] demonstrated that the Fe_3O_4@polydopamine core shell nanocomposites could be applied as therapeutic agents for photothermal anticancer therapy. To date, most of the previous reports were focused on the treatment of tumor cells, while few of them was deal with bacterial [32–34]. Moreover, to better kill the bacterial by photothermal therapy, a relatively high temperature is required, which often limits the practical application. A further improving method that can enhance antibacterial activity without increasing the temperature is highly desired.

In this case, the photodynamic therapy is usually applied as an adjunctive therapy [17,18]. In consideration of the easy conduction and safety, the magnetic field become another wonderful candidate. In previous studies, through hysteresis losses, alternating magnetic fields can allow magnetic particles to be continuously heated, thus enhancing the photothermal effect [35]. This form still essentially enhances by increasing the temperature and does not solve the problem of overheating. Therefore, magnetolytic therapy become an ideal adjunctive therapy because it is based on the magneto-mechanical action of bioorganism and can be coupled with other treatment due to the advantages of safety, convenience, and low cost. It was found that the magnetic particles under alternating magnetic fields, vibrating magnetic fields, or rotating magnetic fields often exerted mechanical force on the surface of the substrate, whatever they were in contact with [36–38]. Due to the unique rotate, oscillate, shear, or other complex motions of the magnetic particles in these applying fields, the generated mechanical forces are sufficient enough to alter the continuity of the surface, which further leads to the onset of apoptosis [15,16,39]. Gao X.H. et al. [40] designed a special structure of magnetic microspheres and firstly proposed the magnetolytic therapy based on magneto-controlled mechanical damage to cell membranes. Cheng Y. et al. [41] designed a zinc-doped iron oxide nanocube, which could effectively target the mitochondria of cancer cells. By means of the rotating magnetic field, the nanocubes assembled in alignment and produced a localized mechanical force to kill the cancer cells. Inspired by this method, many other magnetolytic therapy reagents such as liquid metal [42], porous Fe_3O_4 nanoparticles [43], Ni nanoflowers [13] have been successfully developed. Nevertheless, the bacterial cell walls are stronger compared to cell membranes. The long duration of the magnetic dipole action to bacterial reduces the efficiency of magnetolytic therapy for antibacterial purposes.

It is reported that the Au/Polydopamine (Au/PDA) hybrid layer has excellent photothermal properties and can be coated on the surface of a variety of materials to broaden the application range of the material [17,23,44]. Therefore, by coating the magnetic particles with a shell layer with photothermal properties, a novel candidate with both photothermal and magnetolytic properties will be achieved. Previously, many photothermal nanoplatforms based on magnetic core–shell nanostructure were successfully fabricated. However, none of them concerned about the improvement of the magnetolytic effect on photothermal antibacterial performance. To our knowledge, although the combination of magnetolytic and photothermal therapy is a viable and valuable method in antibacterial, insight into the detail photothermal-magnetolytic coupling antibacterial mechanism is scarce.

In this study, $NiFe_2O_4$@Au/PDA core/shell nanosphere with rough surface has been developed for photothermal-magnetolytic coupling antibacterial performance. Owing to the simple one-step preparation, the shell thickness and Au content can be controlled by changing the experimental conditions. The outer layer endows the nanospheres with an excellent photothermal effect, while the magnetic $NiFe_2O_4$ core offers strong magnetorheological effects. Moreover, the orientation of the magnetolytic is discussed, and the chain model magnetorheological mechanism agrees well with the simulation results. The $NiFe_2O_4$@Au/PDA core/shell nanosphere presents a photothermal antibacterial performance and a typical magnetolytic antibacterial effect. While under the photothermal-magnetolytic coupling treatment, a higher antibacterial efficacy against *Gram-positive* and *Gram-negative bacteria* than either of the individual treatments is observed. This magnetolytic enhancing photothermal antibacterial approach is highly instructive for other multifunctional magnetic nano-agents in treating antimicrobial infections.

2. Materials and methods

2.1. Materials

All chemicals are purchased and used directly without any further purification: Iron (III) chloride hexahydrate ($FeCl_3 \cdot 6H_2O$), Nickel (II) chloride hexahydrate ($NiCl_2 \cdot 6H_2O$), Gold (III) chloride ($HAuCl_4$), Sodium citrate ($C_6H_5Na_3O_7 \cdot 2H_2O$), Urea ($H_2NCONH_2$), Trihydroxymethyl aminomethane (Tris), Ethanol (EtOH), Polyacrylamide (PAM, $[CH_2CH(CONH_2)]_n$), was supplied from Sinopharm Chemical Reagent Co., Ltd. 3-Hydroxytyramine hydrochloride (DA-HCl) was purchased from Aladdin Reagent Co., Ltd. Luria-Bertani Broth and Luria-Bertani agar were purchased from the Hangzhou Microbial Reagent Co., Ltd. *Escherichia coli* (WM3064) and *Staphylococcus aureus* (ATCC6538P) were used for antimicrobial testing. Ultrapure water is used throughout the experiment.

2.2. Preparation of $NiFe_2O_4$ nanospheres

$NiFe_2O_4$ nanospheres were synthesized by an adjusted solvothermal reaction [45]. First, sodium citrate (0.8823 g), $FeCl_3 \cdot 6H_2O$ (0.2703 g), $NiCl_2 \cdot 6H_2O$ (0.1189 g), and urea (0.3603 g) were solubilized in 40 mL ultrapure water. Then, PAM (0.3 g) was dissolved in the solution by sonication at room temperature. After PAM was completely dissolved, the uniform solution was moved and sealed in a stainless-steel autoclave with a Teflon liner and heated to 200 °C for 12 h. Then, the stainless-steel autoclave was cooled to room temperature. The obtained $NiFe_2O_4$ nanospheres were collected from the solution by magnetic separation and washed five times alternately with ethanol and ultrapure water. Finally, $NiFe_2O_4$ nanosphere powder can be gained by freeze-drying the aqueous solution.

2.3. Synthesis of $NiFe_2O_4$@Au/PDA core/shell nanostructure

The monodisperse $NiFe_2O_4$@Au/PDA core/shell nanostructure was prepared by a modified *in situ* redox-oxidize polymerization [46]. Firstly, $NiFe_2O_4$ nanospheres (10 mg) were dispersed in 60 mL ethanol by sonication for 0.5 h. Then, $HAuCl_4$ (0.1 g/mL, 40 μL) and sodium citrate (10 mg) were added to form the solution A. Next, solution B was formed by adding DA-HCl (30 mg) to 30 mL of Tris (pH = 8.5). Then, solution B was added to the A and the reaction was started under ultrasonic conditions. After 3 h of reaction, the product was separated from the solution using magnetic separation. The obtained product was washed alternately with ethanol and ultrapure water, and was freeze-dried to get the final product. In the preparation of different shell thickness and gold content, the other processes remained the same, only the gold or dopamine contents were changed.

2.4. Photothermal effect of $NiFe_2O_4$@Au/PDA

First, the solution of $NiFe_2O_4$@Au/PDA in water at the concentration (1 mg/mL) was prepared and diluted in a gradient dispersion (0, 50, 100, 150 and 200 μg/mL). The absorption value at 808 nm was
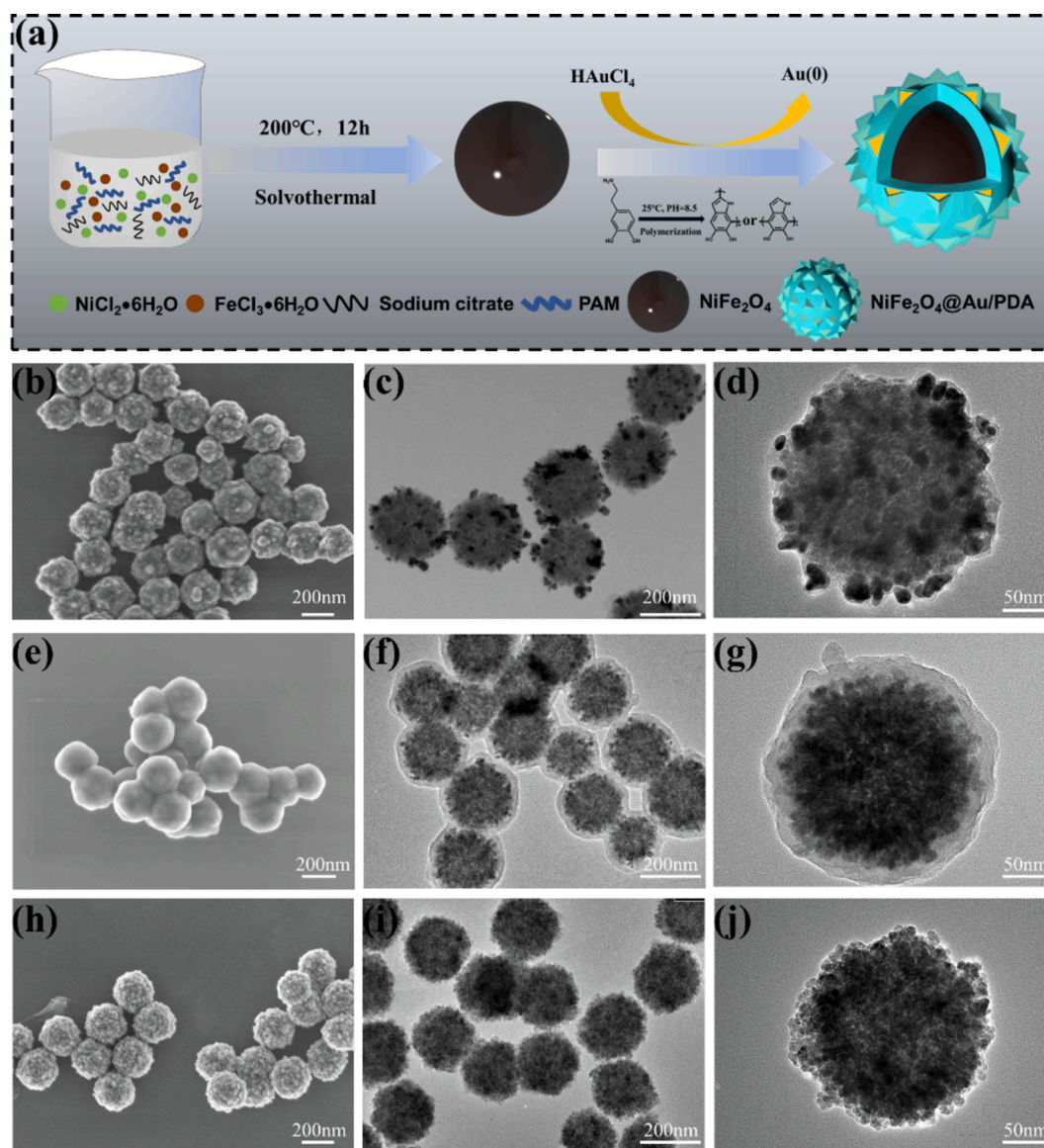
Fig. 1. (a) Scheme for the preparation of NiFe$_2$O$_4$ and NiFe$_2$O$_4$@Au/PDA core/shell nanospheres, SEM (b) and TEM (c, d) images of the NiFe$_2$O$_4$@Au/PDA, SEM (e) and TEM (f, g) images of the NiFe$_2$O$_4$@PDA, and SEM (h) and TEM (i, j) images of the NiFe$_2$O$_4$.

measured. Then, 2 mL of gradient concentrations were added into a centrifuge tube (5 mL) and successively irradiated by NIR light (2.0 W/cm^2) for 10 min. The temperature of the dispersion was recorded every 10 s with the infrared camera and the maximum temperatures of the solution were analyzed. Similarly, the photothermal effect of NiFe$_2$O$_4$ and NiFe$_2$O$_4$@PDA suspensions was tested similar to the NiFe$_2$O$_4$@Au/PDA. Furthermore, the photothermal conversion efficiency was calculated to evaluate the case of the photothermal effect. The details of the formula can be found in the Supporting Information.

2.5. Rheological properties of NiFe$_2$O$_4$@Au/PDA suspension

The NiFe$_2$O$_4$ and NiFe$_2$O$_4$@Au/PDA nanospheres were dispersed into water to form magnetic suspensions with mass fractions of 15, 20 and 25 wt%. The rheological properties of magnetic suspensions were tested by Anton Paar's Physical MCR302. The magnetic suspension is placed between two parallel plates (PP20/MRD) and the rotating upper plate is used to apply the shear force. A uniform magnetic field vertical to the shear direction is generated by a constructed electromagnet. The magnetic field sweep test was performed with the magnetic field linearly

added from 0 to 240 mT at a steady shear rate of 100 s^{-1}. The rheology curves were obtained at constant gradient magnetic fields with shear rates increasing logarithmically from 0.1 to 100 s^{-1}. Microstructures from previous experiments were removed by applying 30 s of pre-shear. The temperature of the test platform was 25 °C at all times during the experiment. The microscopic observation system is described in detail in the text, while the relevant equations for the simulation and information about the fabrication of microfluidic channels can be found in the Supporting Information.

2.6. Antibacterial activity of NiFe$_2$O$_4$@Au/PDA

In order to test the antibacterial activity of the samples, *Escherichia coli* (*E. coli*, Gram-negative bacteria) and *Staphylococcus aureus* (*S. aureus*, Gram-positive bacteria) were selected. Add 50 μL of *E. coli* or *S. aureus* stored in glycerol to 50 mL of fresh Luria-Bertani broth medium in a conical flask and incubate at 37 °C with shaking at 100 rpm for 12 h. Different concentrations of samples were separately injected to *E. coli* or *S. aureus* diluted with fresh Luria-Bertani Broth Medium, and the final concentration of the bacterial solution was 1 × 10^6 CFU/mL. Bacterial
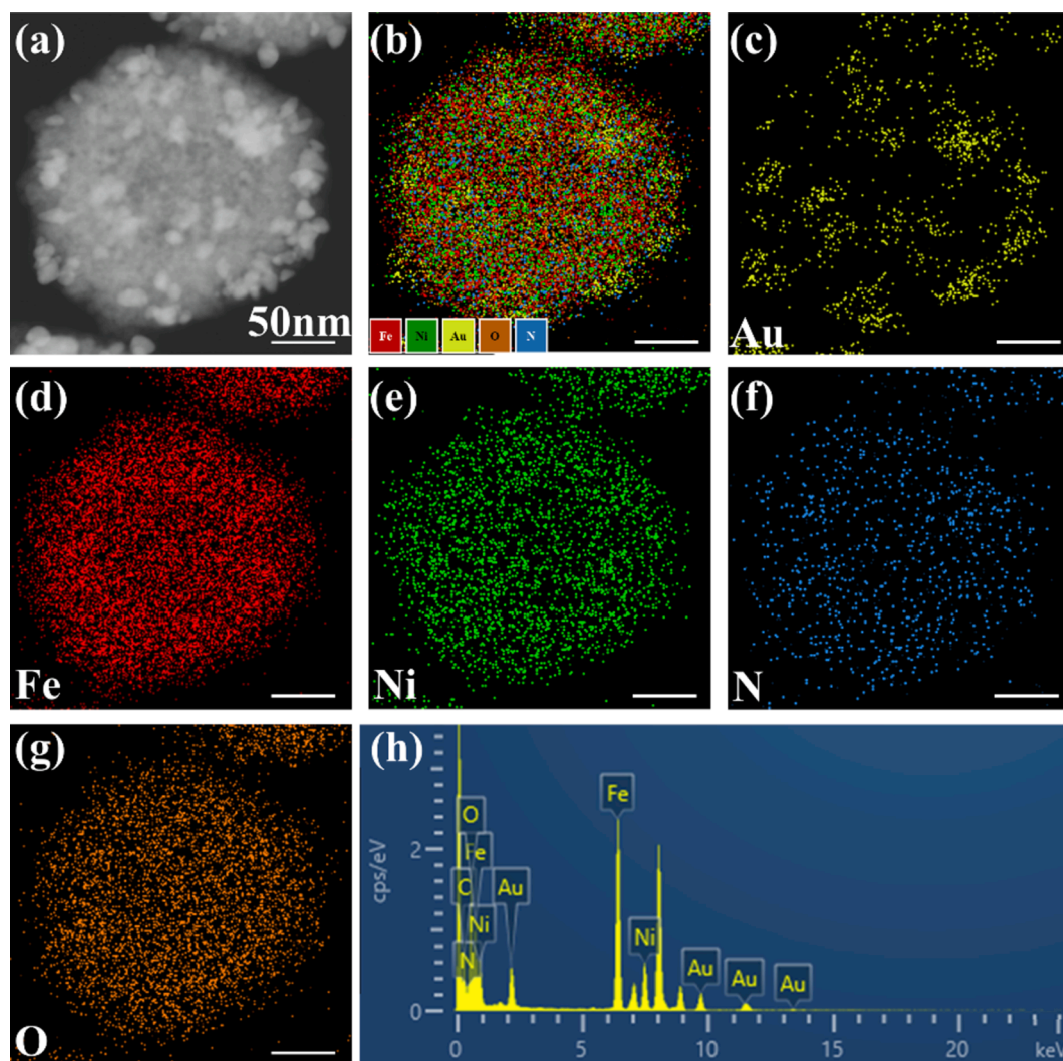
Fig. 2. HAADF-STEM images and EDX elemental mapping of Au, Fe, Ni, N and O (a–g) and the EDX spectrum (h) of the $NiFe_2O_4$@Au/PDA; Scale bar is 50 nm.

suspension was treated with Near-infrared laser (L, 2.0 W/cm^2) and rotating magnetic field (M, 15mT, 200 rpm), and the four groups were labeled as L (+) M (+), L (+) M (-), L (-) M (+), and L (-) M (-), respectively. Except for the control group, the treatment time was 10 min, where L (+) M (+) was the combined action of Near-infrared laser and rotating magnetic field for 10 min. All groups were then incubated in a constant temperature incubator at 37 °C for 4 h. The diluted co-culture solution (100 μL) was then inoculated onto the plate with Luria-Bertani agar medium and incubated at 37 °C for 24 h. Using the dilution assay and the planar colony counting method, the total number of surviving bacteria was measured. SEM imaging analyses were also performed. Detailed procedures are described in the Supporting Information.

2.7. Detection of cytotoxicity using the CCK-8 assay

Human retinal epithelial cells (REP1) were selected for cytotoxicity testing. REP1 cells were seeded into 96-well plates at a cell density of 4 × 10^5 cells/mL. After 24 h of cell culture, the cells were in the logarithmic proliferation phase, with the number of cells accounting for about 85%. Thereafter, the medium was discarded, the sample was added, and the cells were continued to be cultured for 4–72 h. To detect cell viability, the cells were removed and 10 μL of CCK-8 (MCE, USA) solution was added to each well. After incubation in a 5% CO_2 incubator at 37 °C for 45 min, the values were read at 455 nm and 650 nm on an

enzyme marker (BioRad, USA). [A] is obtained by subtracting the reading at 650 nm from the reading at 455 nm. Cell viability was calculated from $[A]_{test}/[A]_{control} \times 100\%$, where $[A]_{test}$ is the absorbance of the complexes and $[A]_{control}$ is the absorbance of the control. Six parallel samples were tested to obtain the average value of absorbance.

2.8. Statistical analysis

All experiments were repeated at three times. Data were presented as means ± standard deviation. Statistical significance was evaluated by using Student *t*-test when only two groups were compared. If more than two groups were compared, evaluation of significance was performed using one-way analysis of variance (ANOVA) followed by Tukey's *post hoc test*. In all tests, statistical significance was set at p less than 0.05.

2.9. Characterization

The sample morphology and nanostructure were characterized by a JEM-2100F field emission transmission electron microscope (FE-TEM) operated at an accelerating voltage of 200 kV. The JEM-2100F also conducted the high-angle annular dark-field scanning TEM (HAADF-STEM) images and energy dispersive X-ray spectroscopy (EDX) elemental maps of the final samples. The field emission scanning electron microscope (FESEM) images were obtained on the Regulus 8230
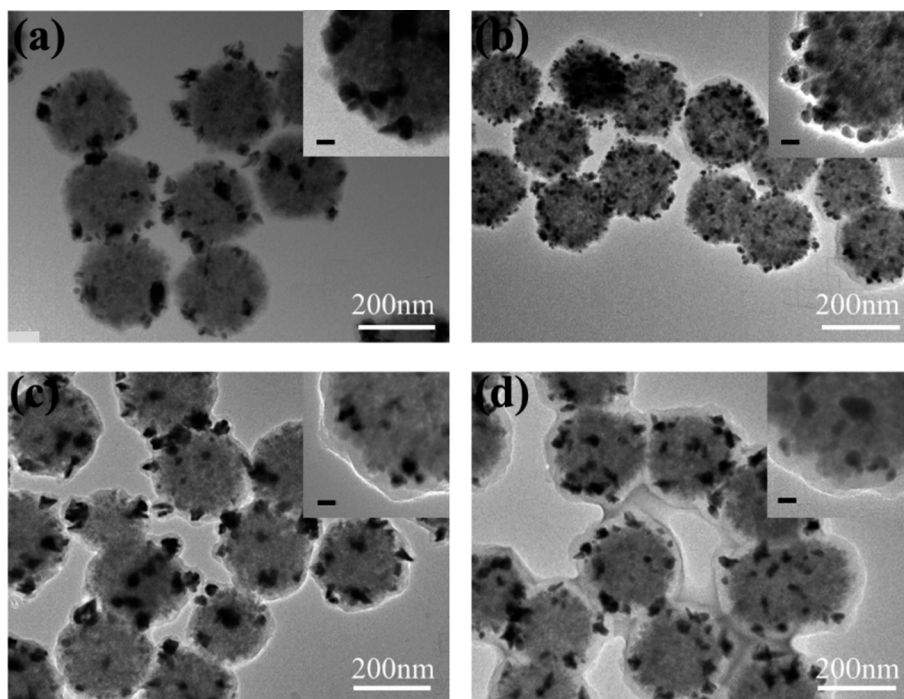
Fig. 3. TEM images of NiFe$_2$O$_4$@Au/PDA prepared with different concentrations of dopamine: 0.2 mg/mL mg (a), 0.3 mg/mL mg (b), 0.7 mg/mL mg (c), and 1.0 mg/mL (d). Insert image scale bar is 20 nm.

HR-FESEM and Sirion 200. X-ray powder diffractograms (XRD) of the nanospheres were obtained with an X-ray diffractometer (Bruker D8 Advance). X-ray photoelectron spectra (XPS) were measured by Electron Spectroscopy (ESCALAB 250). FTIR spectra of all samples in the range of 4000–400 cm^{-1} wavenumber was obtained on an FTIR spectrometer (TENSOR model 27). Thermogravimetric analysis was performed on a thermogravimeter (DTG-60H) heated from room temperature to 800 °C under air conditions at a heating rate of 10 °C/min. Hysteresis loop was measured on a vibrating sample magnetometer (SQUID-VSM) at 300 K. The metal content in the nanospheres was analyzed by using inductively coupled plasma mass spectrometer (ICP-MS, PlasmaQuad 3). Solution temperature during photothermal testing was recorded using an infrared camera (ImageIR 8325).

3. Result and discussion

3.1. Synthesis and characterization of NiFe$_2$O$_4$@Au/PDA core/shell nanosphere

The three-layer NiFe$_2$O$_4$@Au/PDA core/shell nanosphere was successfully prepared by a modified simply *in situ* reduction–oxidation polymerization process [46]. Firstly, as shown in Fig. 1a, the well-dispersed NiFe$_2$O$_4$ nanospheres were obtained by the previously reported solvothermal method [45]. Then, these nanospheres were evenly dispersed in ethanol by ultrasound with the addition of HAuCl$_4$ and sodium citrate. Once the dopamine was added, the dopamine reacted rapidly with the HAuCl$_4$ to form Au/Polydopamine (Au/PDA) hybrid and covered on the surface of NiFe$_2$O$_4$ nanosphere to form the NiFe$_2$O$_4$@Au/PDA core shell nanostructure [47]. As shown in Fig. 1b, the synthesized samples exhibit a uniform spherical morphology and the average particle size of finally NiFe$_2$O$_4$@Au/PDA is about 250 nm. The TEM image agrees that the size of the nanospheres is relatively homogeneous (Fig. 1c). The high magnification TEM image (Fig. 1d) indicates the NiFe$_2$O$_4$@Au/PDA core/shell nanospheres own a three-layer nanostructure. Between the continuous inner NiFe$_2$O$_4$ core and the external thin PDA crust layer, there exist a lot of grainy protrusion, which are the Au nanocrystals. Typically, the exterior pale PDA shell well encapsulate

all of the Au nanocrystals. In comparison to the original NiFe$_2$O$_4$ nanosphere (Fig. 1h-j), the surface of the NiFe$_2$O$_4$@Au/PDA is much rough, mainly because of the outer hybrid coating layer. Here, without adding the HAuCl$_4$, only NiFe$_2$O$_4$@PDA nanospheres with core shell nanostructure are obtained after a 12 h coating reaction (Fig. 1e–g). In this work, the preparation time for NiFe$_2$O$_4$@Au/PDA is 3 h, thus the thickness of the PDA layer is thin and is believed to be favored for the uneven surface. This rough surface NiFe$_2$O$_4$@Au/PDA nanosphere is more likely to lead to concentrated stress at the peak. This structure characteristic is helpful for improving the magnetolytic effect under applying the external magnetic field.

In comparison to the original NiFe$_2$O$_4$, the average size of the NiFe$_2$O$_4$@Au/PDA is about 40 nm larger, which is certainly due to the presence of the Au/PDA hybrid coating layer (Fig. S2a, b). The HAADF-STEM images and EDX elemental maps were used to investigate the composition of the NiFe$_2$O$_4$@Au/PDA core/shell nanosphere. Obviously, the core/shell nanostructure is mainly composed of Au, Fe, Ni, C, N and O (Fig. 2h). Typically, the Fe and Ni are well distributed in the center of the nanospheres, where Fe is denser than Ni (Fig. 2a-e). Interestingly, the Au element (Fig. 2c) is non-uniformly distributed on the surface of the NiFe$_2$O$_4$ nanosphere with a larger diameter than the Fe and Ni component map, which demonstrates that the Au element forms crystalline nanocrystals and they are covered on the periphery of the NiFe$_2$O$_4$ nanosphere. Moreover, although the diameter of the Au map is about 40–50 nm larger than Fe and Ni, it is smaller than N and O [46] (Fig. 2f-g), indicating that the Au nanocrystals are sandwiched between the NiFe$_2$O$_4$ core and the PDA layer, which agrees with the TEM analysis. Based on the above analysis, it can be derived that the as-prepared NiFe$_2$O$_4$@Au/PDA nanosphere presents a sandwich-like nanostructure with a 200 nm NiFe$_2$O$_4$ core and the 20 nm thickness Au/PDA hybrid layer.

The internal nanostructure of the NiFe$_2$O$_4$@Au/PDA can be easily adjusted by altering the concentration of dopamine and HAuCl$_4$. As shown in Fig. 3, the shell thickness of the Au/PDA hybrid layer is related to the concentration of dopamine. Keeping the HAuCl$_4$ concentration as a constant, the thicknesses of Au/PDA change from 10 to 35 nm as the concentrations of the dopamine increase from 0.2 mg/mL to 1.0 mg/mL.
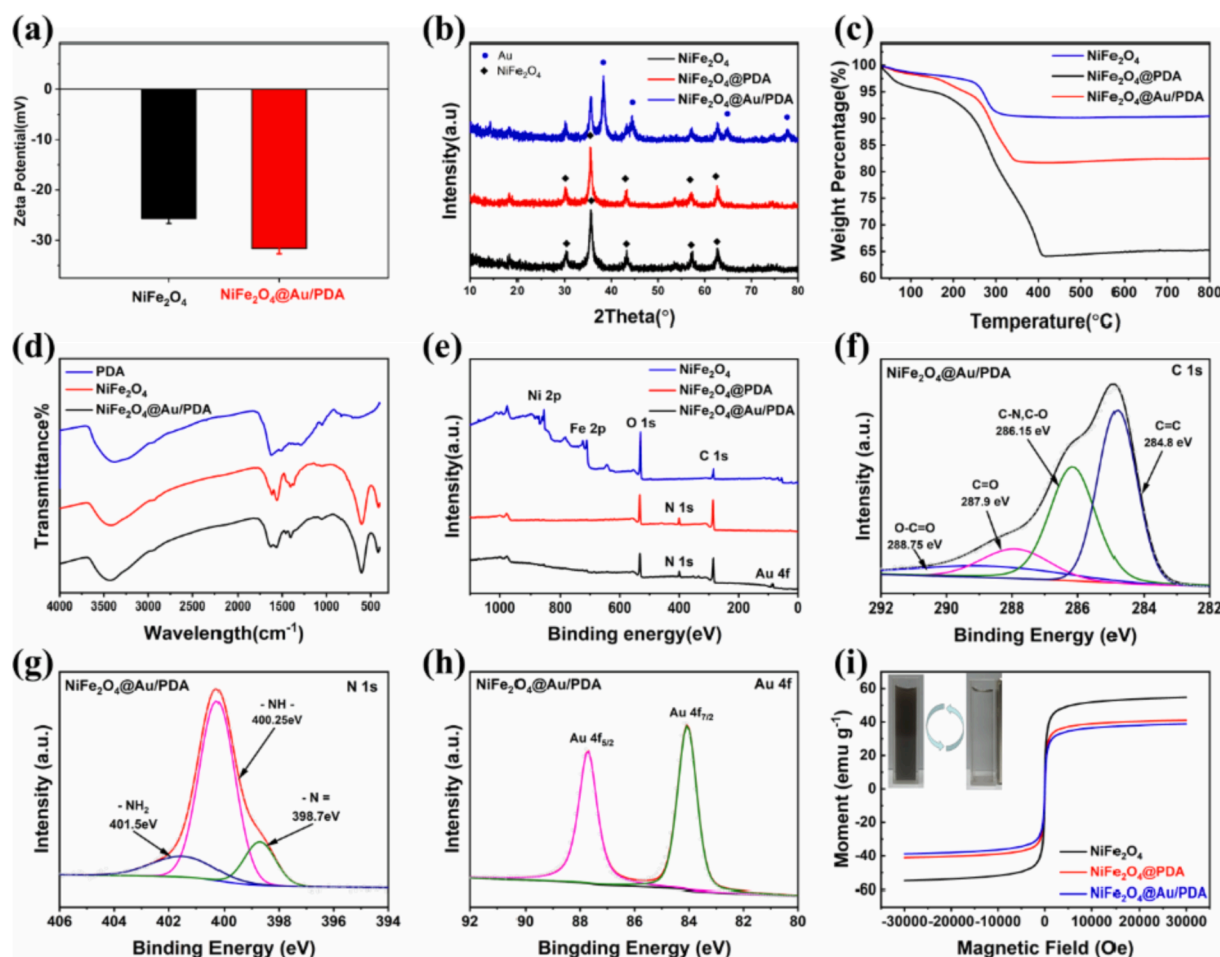
Fig. 4. (a) Zeta potential, (b) XRD diffraction patterns, (c) TG curves, (e) XPS spectra and (i) magnetization hysteresis loops of the $NiFe_2O_4$, $NiFe_2O_4$@PDA and $NiFe_2O_4$@Au/PDA nanospheres; (d) FTIR spectra of PDA, $NiFe_2O_4$, $NiFe_2O_4$@Au/PDA; (f) C 1 s, (g) N 1 s and (h) Au 4f core-level spectra of $NiFe_2O_4$ @ Au/PDA.

In this work, with rising dopamine concentration, the Au nanocrystals will be continually coated with polydopamine, thus the surface of the $NiFe_2O_4$@Au/PDA particles tend to be smooth, just like the $NiFe_2O_4$@PDA case. To achieve a rough surface, the dopamine concentration is kept at 0.3 mg/mL. As shown in Fig. S3, when the DA concentration is kept, with the concentration of $HAuCl_4$ increasing from 6.5×10^{-5} M to 2.6×10^{-4} M, the number and size of Au increase correspondingly. The thin PDA shell layer is bad for Au shedding and too thick PDA coating leads to a smooth surface which is un-conducive for magnetolytic action. As a result, 0.3 mg/mL PDA and 2.6×10^{-4} M $HAuCl_4$ are the optimum conditions for preparing $NiFe_2O_4$@Au/PDA nanospheres.

After wrapping the Au/PDA shell layer, the surface of the $NiFe_2O_4$ nanosphere critically changed. As shown in Fig. 4a, the Zeta potential of the final product decreased, leading to enhancing stability in solution. The XRD patterns of $NiFe_2O_4$, $NiFe_2O_4$@PDA and $NiFe_2O_4$@Au/PDA nanospheres are shown in Fig. 4b. The $NiFe_2O_4$ nanospheres present a classic face-centered cubic phase (JCPDS Card No. 23–1119). Because the nanosphere is composed of secondary nanocrystals, the diffraction peaks are relatively broad. After the Au/PDA shell is covered on the $NiFe_2O_4$ nanosphere, four additional broad peaks occur at 38.0°, 44.0°, 64.7° and 77.6°, which can be classified as (111), (200), (220), and (311) of the Au lattice plane (JCPDS Card NO. 04–0784). No additional peak of impurity is found in the XRD patterns, which means that the Au/PDA cladding procedure does not affect the crystal structure of original $NiFe_2O_4$. The element composition determined by ICP-MS also indicates that the Ni and Fe weight ratios are reduced in the $NiFe_2O_4$@Au/PDA, which further proves the coating of the Au/PDA (Table S1). Since PDA

polymer is amorphous, XRD patterns cannot be used to detect PDA.

Thermogravimetric (TG) analysis is further used for studying the composition of the $NiFe_2O_4$@Au/PDA nanospheres. The weight losses of $NiFe_2O_4$, $NiFe_2O_4$@PDA and $NiFe_2O_4$@Au/PDA are 9.58 wt%, 34.71 wt % and 17.52 wt%, respectively (Fig. 4c). It is obvious that the increase in weight loss must come from the decomposition of the PDA at high temperatures. Because Au nanocrystals cannot be decomposed at high temperatures, the weight loss of $NiFe_2O_4$@Au/PDA is less than $NiFe_2O_4$@PDA. This result indicates that Au occupies a large portion of the weight in the Au/PDA shell. Fig. 4d shows the FT-IR spectra of each sample in the range of 4000–400 cm^{-1}. Two main metal–oxygen bands at 602 cm^{-1} and 409 cm^{-1} are observed and they are attributed from the $NiFe_2O_4$ nanospheres. For the $NiFe_2O_4$@Au/PDA, the pronounced peaks at 3367, 1629, and 1276 cm^{-1} are assigned to the $-OH/-NH_2$, C = O, and C-N stretching vibration of PDA. XPS was applied to further study the surface elemental composition of $NiFe_2O_4$@Au/PDA nanospheres. As shown in Fig. 4e, O 1 s (530.4 eV), Ni 2p (855.4 eV) and Fe 2p (710.4 eV) peaks are obvious in spectra of $NiFe_2O_4$. Here, the tiny peak at C 1 s (284.4 eV) must be originated from the ethanol or remaining polyacrylamide chains [44]. After coating the Au/PDA shells, Ni 2p and Fe 2p peaks are almost un-observable, and N 1 s (400.3 eV) and Au 4f (84.1 and 87.7 eV) appear in the spectrum. The characteristic C-N peak at 286.2 eV in the C 1 s spectrum occupies a significant proportion (Fig. 4f). Since the element N is presented only with PDA, thus the N 1 s spectrum (Fig. 4g) shows three peaks at 398.7, 400.1 and 401.5 eV, and they are assigning to tertiary/aromatic (-N-), secondary (–NH-) and primary amine ($-NH_2$) groups of PDA, respectively. Moreover, the Au is completely in the singlet state with no additional satellite peaks. Since
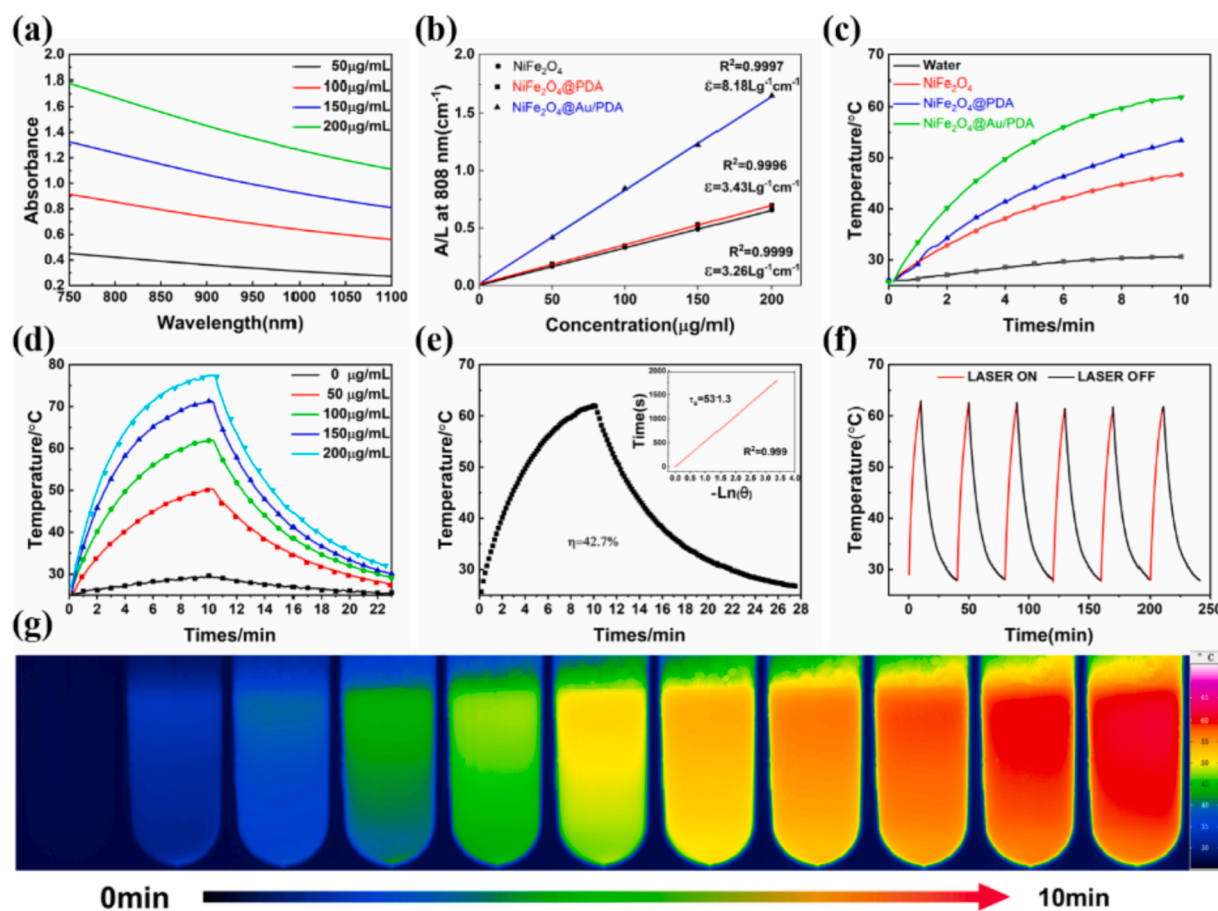
Fig. 5. Photothermal-property characterization of NiFe$_2$O$_4$@Au/PDA under 808 nm NIR irradiation (2.0 W/cm^2). (a) UV–vis spectra of different concentrations of NiFe$_2$O$_4$@Au/PDA dispersed in aqueous solution; (b) The extinction coefficient and (c) Temperature elevation curves (100 μg/mL) of DI water, NiFe$_2$O$_4$, NiFe$_2$O$_4$@PDA, NiFe$_2$O$_4$@Au/PDA; (d) Temperature elevation of NiFe$_2$O$_4$@Au/PDA with different concentrations; (e) Temperature elevation curves of NiFe$_2$O$_4$@Au/PDA dispersions (100 μg/mL) after continuous irradiation and natural cooling and a plot fitting of cooling time versus -ln(θ) (inset graph); (f) Recycling-heating profiles of NiFe$_2$O$_4$@Au/PDA aqueous solution (100 μg/mL) for six on/off cycles; (g) The infrared thermal image of NiFe$_2$O$_4$@Au/PDA (100 μg/mL) suspension.

the detection depth of XPS is about 10 nm, the finding of Au elements indicates a very thin PDA layer on the NiFe$_2$O$_4$@Au/PDA nanosphere. Based on the above analysis, it can be determined that the magnetic NiFe$_2$O$_4$ spheres are functionalized by Au/PDA shells.

In this work, the NiFe$_2$O$_4$ nanospheres are chosen as the core template beyond the traditionally used Fe$_3$O$_4$, for the former usually shows higher stability than the latter. The hysteresis loops of NiFe$_2$O$_4$, NiFe$_2$O$_4$@PDA and NiFe$_2$O$_4$@Au/PDA nanospheres were measured by SQUID-VSM at 300 K (Fig. 4i) and the internal illustration showed the typical magnetic separation properties of NiFe$_2$O$_4$@Au/PDA nanospheres. Because the NiFe$_2$O$_4$ core is composed of a large number of small secondary nanograins, both the NiFe$_2$O$_4$ and NiFe$_2$O$_4$@Au/PDA exhibit unique superparamagnetic properties. The saturation magnetizations of NiFe$_2$O$_4$@Au/PDA (38.9 emu/g) and NiFe$_2$O$_4$@PDA (41.1 emu/g) nanospheres are smaller than that of pristine NiFe$_2$O$_4$ (54.8 emu/g) due to the presence of the shell. However, it is still strong enough to perform magnetic separation (the upper left inset of Fig. 4i).

3.2. The photothermal effect and magneto-mechanic behavior of NiFe$_2$O$_4$@Au/PDA

Due to the existence of Au and PDA, the NiFe$_2$O$_4$@Au/PDA is expected to exhibit excellent photothermal effect. Fig. S4 shows the photothermal performance testing device, which is used to characterize the photothermal performance of the prepared samples by recording the change of solution temperature at different times. Because

NiFe$_2$O$_4$@Au/PDA has low Zeta potential, it can be efficiently dispersed in ultrapure water. The aqueous solution exhibits a broad absorption spectrum of NIR-I from 780 to 1100 nm with a low concentration (Fig. 5a, Fig. S5, d). The extinction coefficient was calculated according to formula 1 in Supporting Information. It can be seen that A/L has a wonderful linear relationship with concentration due to the Lambert-Beer law. The results of extinction coefficient of the products at 808 nm are 3.26, 3.43 and 17.3 Lg^{-1}·cm^{-1}, respectively, indicating a high absorption at 808 nm (Fig. 5b). As shown in Fig. 5c, after 10 min of NIR irradiation (808 nm, 2 W/cm^2), the temperature of NiFe$_2$O$_4$@Au/PDA solutions (2 mL, 100 μg/mL) rises rapidly from 25.0 °C to 61.8 °C. As a comparison, the temperature of the DI increases less than 5 °C. All the aqueous solutions possessed a concentration-dependent photothermal effect when irradiated at fixed energy (Fig. 5d, Fig. S5b, e). Obviously, the NiFe$_2$O$_4$@Au/PDA core shell nanosphere exhibits a superior photothermal effect due to the presence of PDA and Au. In addition, the photothermal performance of NiFe$_2$O$_4$@Au/PDA is linearly related to the laser power density. The maximum temperature increases significantly with increasing of the laser power density (Figure S6). However, when the power is reduced to 1.0 W/cm^2, the suspension still possesses nearly 50 °C, which also shows a good photothermal performance.

To further understand the main functions of each part, after 10 min irradiation, the aqueous solution (100 μg/mL) was cooled to room temperature, and the photothermal conversion efficiency was calculated according to formula 2 in Supporting Information. The conversion efficiency values of NiFe$_2$O$_4$ and NiFe$_2$O$_4$@PDA are 25.5 % and 34.3 %,

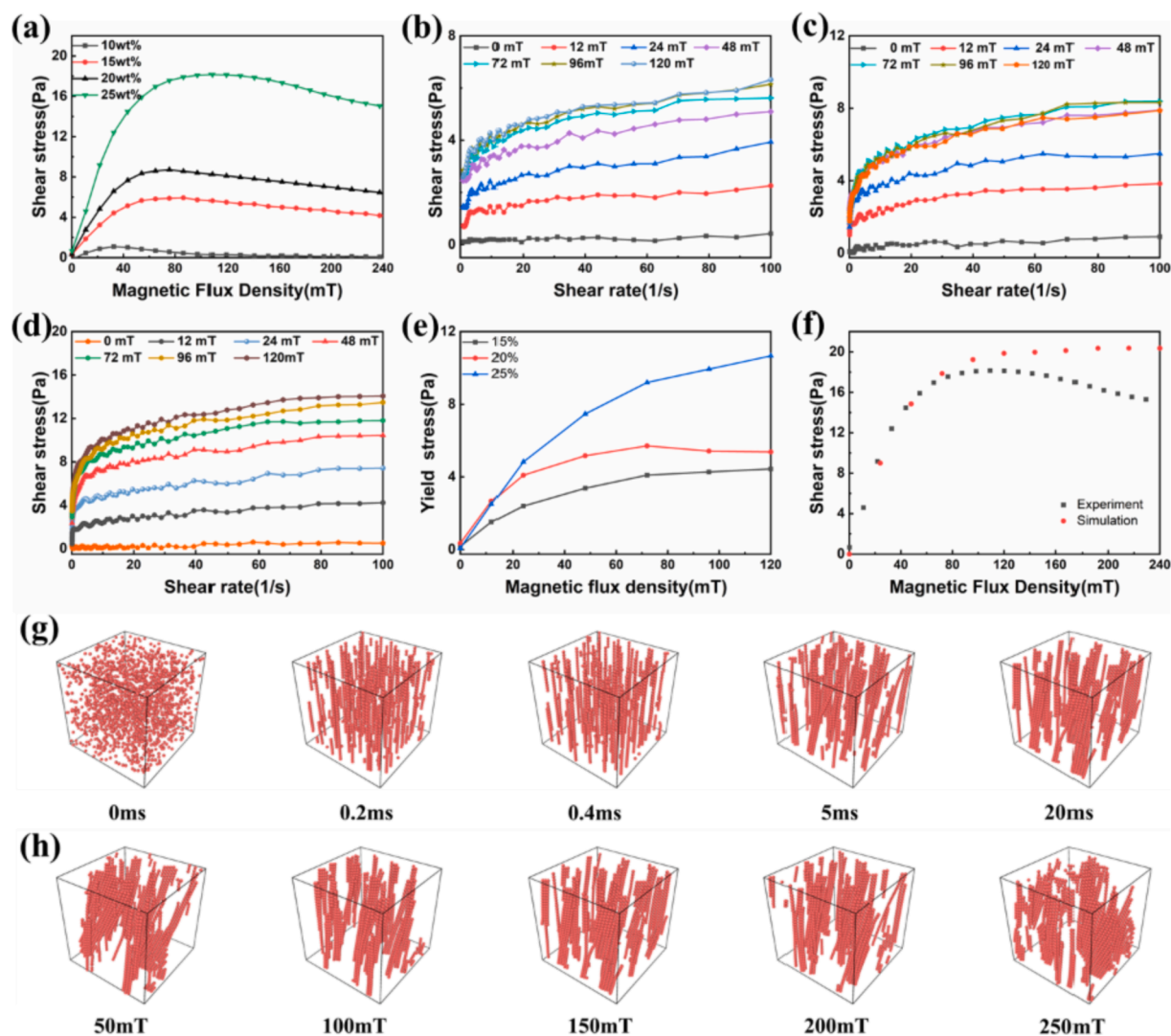**Fig. 6.** Rheological properties of NiFe$_2$O$_4$@Au/PDA based magnetic suspensions. (a) Magnetic field sweep test; Magnetic suspension flow curves of various mass fractions under different magnetic fields: (b) 15 wt%, (c) 20 wt%, and (d) 25 wt%;(e) Static yield stress versus external magnetic field; (f) Comparison of experimental and simulated results of magnetic field sweep test (25 wt%); (g) Evolution of microstructures of 15 wt% magnetic suspension; (h) Microstructure of different magnetic fields at the end of the simulation.

while the NiFe$_2$O$_4$@Au/PDA core–shell nanosphere reaches 42.7 %, (Fig. 5e, Fig. S4c, f). In comparison to the gold nanoflowers (74%) and gold nanoplates (68.5%), the photothermal conversion of NiFe$_2$O$_4$@Au/PDA nanospheres is lower [48]. However, this photothermal conversion efficiency of our product is as high as other normal used photothermal nanomaterials [48]. This is due to the fact that both PDA and Au nanocrystals play a critical role in photothermal conversion, as near-infrared light needs to pass through a PDA shell layer before the gold nanoparticles can act, so the photothermal conversion efficiency is bound to be discounted. The photothermal stability of NiFe$_2$O$_4$@Au/PDA was evaluated by heating the sample (100 µg/mL) with the NIR laser on and off at room-temperature. Fluctuations in the temperature profile and the maximum temperature of the sample suspension during the subsequent five cycles were negligible compared to the temperature changes during the first heating and cooling cycle (Fig. 5f), which indicated that the NiFe$_2$O$_4$@Au/PDA possesses good photothermal stability. The infrared thermal images (Fig. 5g) of the sample suspension were also recorded by an infrared thermal camera every 60 s. With the extension of illumination time, the temperature increased significantly.

Originated from the superparamagnetic NiFe$_2$O$_4$, the NiFe$_2$O$_4$@Au/PDA nanospheres are forced to move under applying the external

magnetic field. The magneto-mechanic behavior of NiFe$_2$O$_4$@Au/PDA was also investigated by testing the rheological properties of the magnetic NiFe$_2$O$_4$@Au/PDA suspension (Fig. 6). As shown in Fig. 6a, the physical state of the magnetic suspension gradually changed with the increasing of the magnetic field intensity. Typically, the shear stress increases with the increasing of magnetic flux density. Once the magnetic flux density exceeds a critical level, the shear stress of the magnetic suspension decreases. This trend is more pronounced in dilute magnetic suspension (10–15 wt%), while for higher concentrations of magnetic suspension (20–25 wt%), the shear stress reaches a relatively flat state after reaching saturation magnetization. Under an external magnetic field, the NiFe$_2$O$_4$@Au/PDA nanospheres are magnetized and the magnetic dipole–dipole interaction forces the nanospheres to form chains-like microstructure along the magnetic field. In this case, the shear stress will be increased due to the as-named magnetorheological effect. Due to the microstructure tilting toward the shear direction in a steady shear flow, a continuous process of destruction and reorganization will be acquired. However, the testing magnetic field is not perfectly uniform and the gravity cannot be neglected, the NiFe$_2$O$_4$@Au/PDA nanospheres tend to be attracted to one shear plane. Thus, the shear stress decreases for the low concentration magnetic suspension.
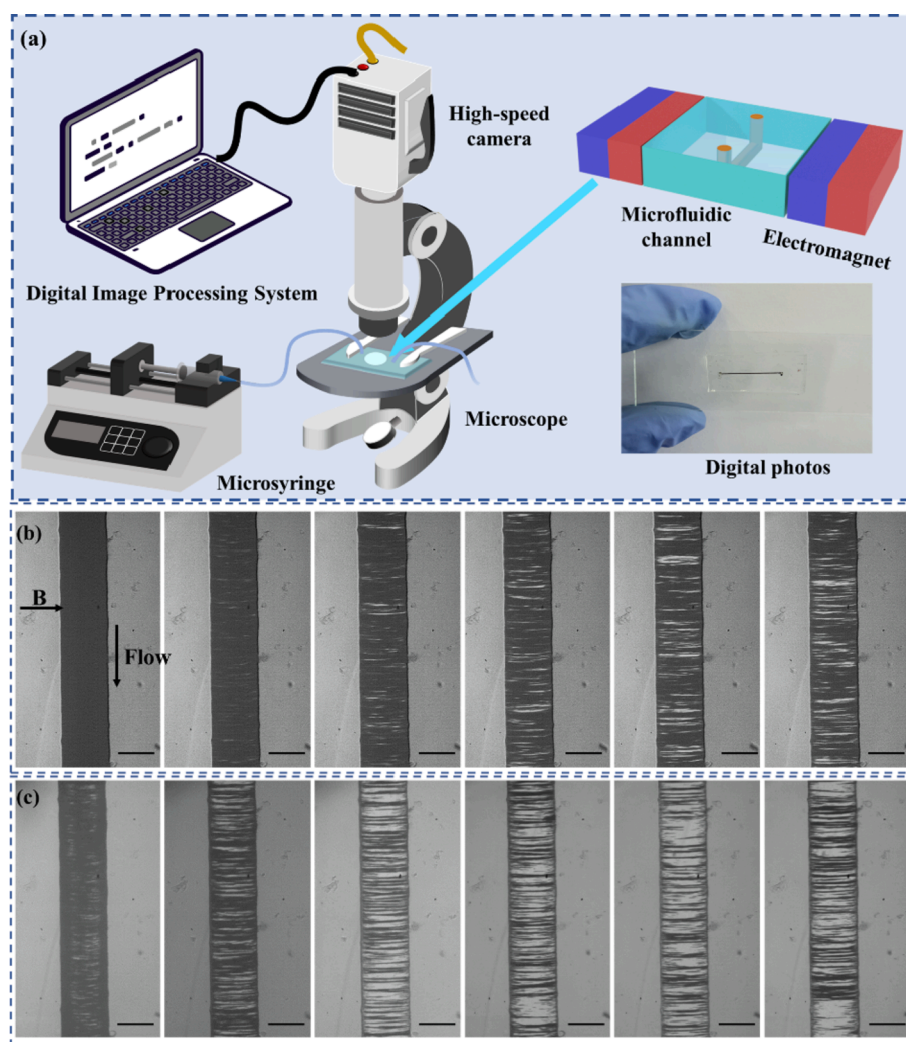
Fig.7. (a) Microscopic observation device structure schematic diagram; (b) The microstructures corresponding to different times (from left to right: 0, 200 ms, 400 ms, 600 ms, 800 ms, 1000 ms) after turning on the magnetic field; (c) Microstructures at different magnetic fields when the liquid flow is stable (from left to right: 5 mT, 10 mT, 15 mT, 20 mT, 25 mT, 30 mT). Scale bar is 200 μm.

Fig. 6b-d show the shear stress curves of magnetic suspensions with different mass fractions as the magnetic field changes. Without applying external magnetic field, $NiFe_2O_4$@Au/PDA is uniformly distributed in the suspension and does not affect the shear stress, similar to a typical Newtonian fluid. After loading the magnetic field, the chain-like microstructures are formed. When the sample is forced to flow, the shear load should first overcome the original microstructure, at which point the magnetic suspension exhibits a static yield stress τ_0. If the stress is less than τ_0, the suspension will be assumed as a solid-like state. When the shear stress exceeds this value, the magnetic suspension is in a flowing state and exhibits a liquid property. At high shear rates, typical Bingham characteristics can be observed. The flow curves can be described as:

$$\tau = \tau_0 + \eta_p \dot{\gamma} \tag{1}$$

where τ is the shear stress, η_p is the zero-field viscosity at high shear rates independent of the magnetic field, τ_0 is the static yield stress of magnetic suspension, and $\dot{\gamma}$ is the shear strain rate. Based on the equation, it can be found that the shear stress should always increase with increasing of the magnetic field until saturation. Fig. 6e shows that τ_0 increases with advancing external magnetic field and the sample concentration, mainly determined by the number of microstructures. By comparing the properties with those of the magnetic suspension formulated with $NiFe_2O_4$, it can be seen that the difference between the

magnetorheological properties of the two is not significant, despite the decrease in saturation magnetization intensity (Fig. S7). This may be mainly due to the similar magnetic behavior of the particles. In this work, it is found that increases of the interaction between particles often lead to the formation of a stronger chain of particles. Therefore, the high concentration $NiFe_2O_4$@Au/PDA suspension will exhibit a stronger magneto-mechanic behavior.

To better understand the magneto-mechanic behavior mechanism of $NiFe_2O_4$@Au/PDA magnetic suspension, the microstructural evolution of the magnetic suspensions is simulated by OVITO software using a Molecule Dynamic method [49] (Fig. 6g). First, a stable homogeneous magnetic field with B = 150 mT is chosen, and the mass fraction and shear rate of the magnetic suspension is set at 15 wt% and 100 s^{-1}. In the original state, $NiFe_2O_4$@Au/PDA nanospheres are uniformly distributed in the simulation chamber. Under applying both of a shear force and an external magnetic field, the particles rapidly (0.2 ms) develop short chains following the magnetic field direction because of magnetic dipole–dipole interaction. In a concise time (0.4 ms), the short chains continue to assemble and arrange each other to form a longer chain. Due to the loading of the shear flow, the microstructure tilts in different directions at 5 ms. The inclination angle of the chain is relatively small. Eventually, the X-directional component of the force loaded by the magnetic field is balanced with the hydrodynamic forces from substrate. When the simulated process reaches dynamic equilibrium (20 ms), these
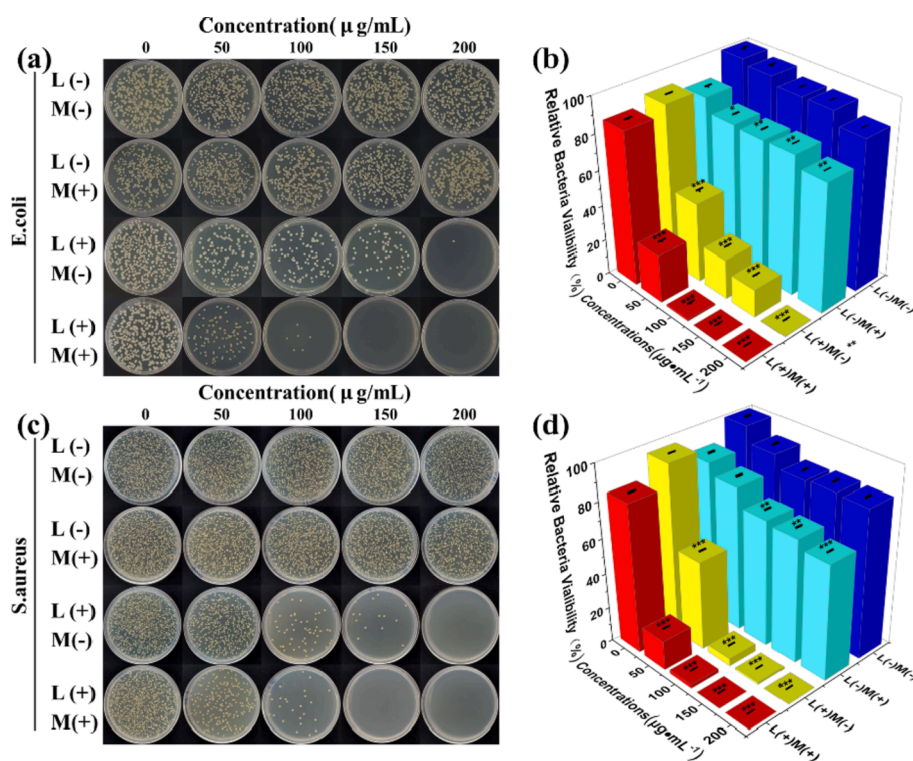
Fig. 8. Image of bacterial colonies formed by (a) *E. coli*, and (c) *S. aureus* treated with NiFe$_2$O$_4$@Au/PDA (0, 50, 100, 150, and 200 µg/mL) with or without NIR irradiation and rotating magnetic field for 10 min (Near-infrared laser (L, 2.0 W/cm^2) and rotating magnetic field (M, 15mT, 200 rpm)). The corresponding bacterial viabilities of (b) *E. coli*, and (d) *S. aureus* after treatment with NiFe$_2$O$_4$@Au/PDA in different groups determined by the plate counting method. N = 3 for all samples.

chains do not flow with the substrate or further assemble into other new microstructures during the rest of the simulated process.

Fig. 6h shows the dynamic equilibrium microstructure at different external fields at the same shear rate. In a weak magnetic field (50 mT), the chain-like microstructure has a consistent oblique angle toward the X-axis (shear direction). As the external field increases, the inclination of the chains decreases and becomes irregular. When the magnetic field strength is over 150 mT, the microstructure shows a similar feature. The X-component of the magnetic dipole force is positively correlated with the magnetic flux density. The stronger the external magnetic field, the smaller the inclination angle of the chain is needed to counteract the shear force. The comparison between experiments and simulations of shear stress *vs* external magnetic field is shown in Fig. 6f. The simulation results are higher than the experimental results due to the simulation did not take settlement into account. Basically, based on the above analysis, it can be concluded that the simulation matches well with experiment.

To further verify the inference, the Microfluidic device experimental setup is used to observe the magnetic suspension microstructure in Poiseuille flow (Fig. 7a). The microscopic observation device consists of a microscopic imaging device, a high-speed photography system, an injection system, a magnetic field control device and a microfluidic channel. Using soft lithography techniques, microfluidic channels with rectangular cross sections were fabricated. Two parallel electromagnets were used to produce a uniform magnetic field, and the strength of the uniform magnetic field was tuned by regulating the magnitude of the current. The mass fraction of magnetic suspension was 10 wt%. The streaming rate was fixed at 0.3 mL/h and the high-speed camera had a frame rate of 10,000. With increasing applying time of magnetic field, the NiFe$_2$O$_4$@Au/PDA chains gradually form a column-mounted structure almost parallel to the magnetic field (Fig. 8b), while the thickness becomes stable. Due to the non-uniform velocity of the substrate in the channel, these columns often overtake each other (Video S1). Fig. 8c shows that the column-mounted structure parallel to the magnetic field is getting thicker as the strength of the magnetic field flux increases.

Therefore, for better magneto-mechanic effect, the strength of the magnetic field should not be too high when applying the magnetic field. A lower magnetic field not only reduces the side effects but also increases the concentrated stress. As a result, the probability of acting on the bacteria becomes large due to the formation of finer and more granular chains.

3.3. The photothermal-magnetolytic coupling antibacterial performance of NiFe$_2$O$_4$@Au/PDA

Owing to the wonderful photothermal characteristic and magneto-mechanic behavior, the NiFe$_2$O$_4$@Au/PDA core/shell nanospheres show high potential in biology. To explore the broad-spectrum antimicrobial properties of the above materials, Gram-negative bacteria (*E. coli*) and Gram-positive bacteria (*S. aureus*) were selected to assess the antibacterial capacity.

The antibacterial performance of the NiFe$_2$O$_4$@Au/PDA nanospheres is measured under four different processes: no-action, photothermal, magnetic, and photothermal-magnetolytic coupling. The images of *E. coli* and *S. aureus* treated with different conditions of NiFe$_2$O$_4$@Au/PDA and the final histogram of antibacterial effect are shown in Fig. 8. It can be seen that the antibacterial properties of NiFe$_2$O$_4$@Au/PDA for both *E. coli* and *S. aureus* almost show the same trend, in which the antibacterial effect becomes more and more effective with increasing of the concentration and coordinated action. Fig. 8a and 8b show that the top row of Petri dishes filled with *E. coli* or *S. aureus*, indicating that NiFe$_2$O$_4$@Au/PDA possesses a very weak antibacterial effect without any external treatment. When the rotating magnetic field is applied, the dishes are still filled with *E. coli* or *S. aureus*. Interestingly, the statistics show that the bacterial activity is still reduced in comparison to the control group, indicating that the magnetic field still has some antibacterial effect. With pure NIR irradiation, the growth of *E. coli* and *S. aureus* is significantly inhibited and the survival rate is drastically reduced, similar to most of the previous reports [19,29,48]. In this work,
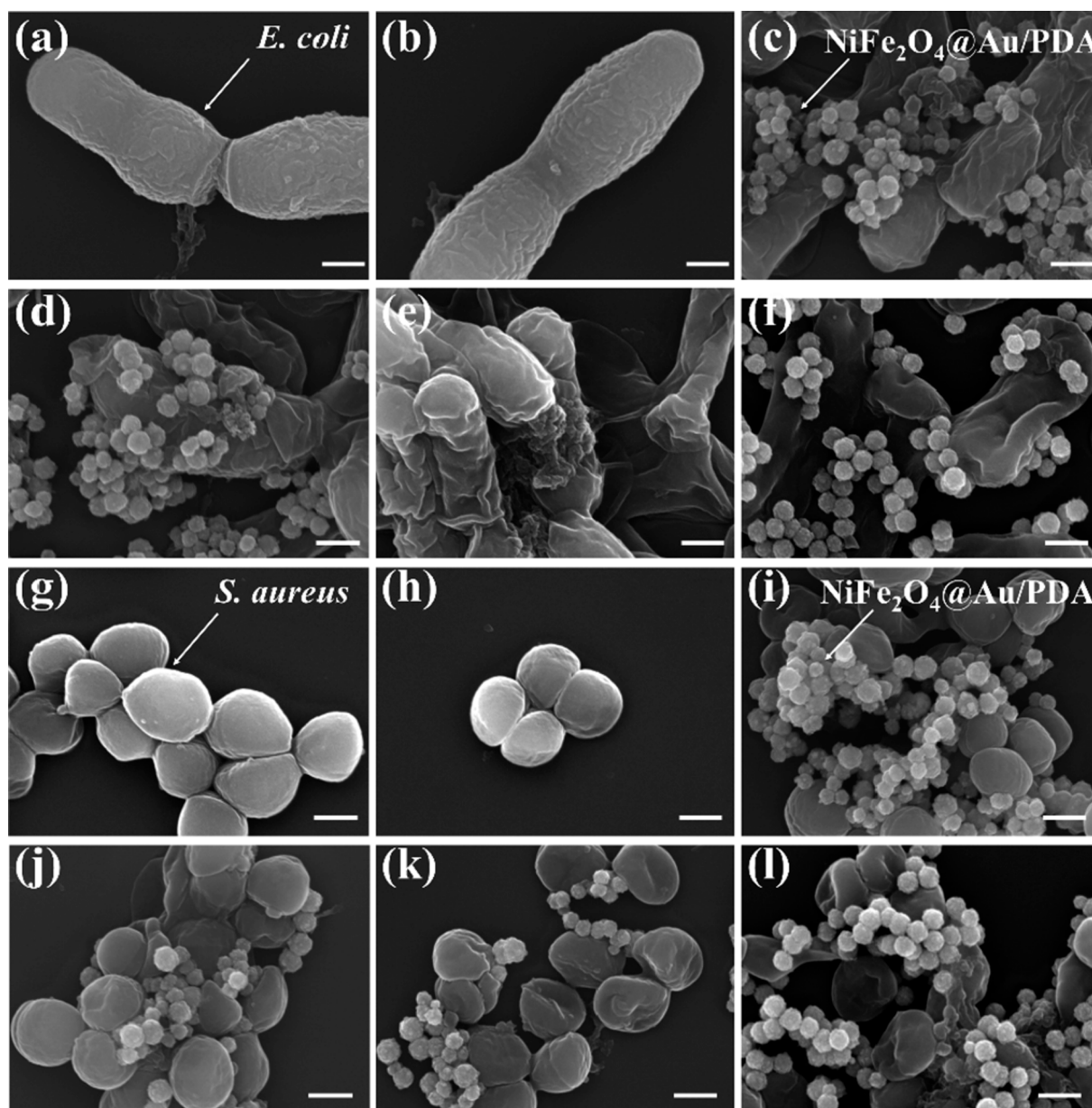
Fig. 9. FESEM images of *E. coli* and *S. aureus* after different treatments with NiFe$_2$O$_4$@Au/PDA (200 μg/mL) (a) and (g) control, (b) and (h) NIR, (c) and (i) NiFe$_2$O$_4$@Au/PDA, (d) and (j) NiFe$_2$O$_4$@Au/PDA + Rotating magnetic field, (e) and (k) NiFe$_2$O$_4$@Au/PDA + NIR, (f) and (l) NiFe$_2$O$_4$@Au/PDA + NIR + Rotating magnetic field. Scale bar is 500 nm.

the antibacterial experiments have also been conducted under both applying the near-infrared light and the rotating magnetic field. As shown in Fig. 8, the antibacterial effect is the best under this coupling treatment. In comparison to the pure NIR, the photothermal-magnetolytic therapy exhibits a much higher effect, which demonstrates an interesting photothermal-magnetolytic coupling anti-bacterial performance.

To optimize the treatment, detailed experiment conditions are discussed. When the concentration of NiFe$_2$O$_4$@Au/PDA is kept at 50 μg/mL, more than half of the bacteria are inactivated under NIR irradiation. When the concentration reaches 200 μg/mL, all bacteria are inactivated, indicating a good photothermal antibacterial performance. In this case, if the rotating magnetic field is simultaneous acted under the NIR irradiation, the NiFe$_2$O$_4$@Au/PDA concentration for complete antibacterial will drop to 150 μg/mL (Fig. 8c, d). As discussed in the above photothermal behavior, the temperature of this photothermal-magnetolytic coupling anti-bacterial process can simultaneously reduce about 7–8

°C for the solution, which will be safer. Therefore, in comparison to the sole near-infrared light irradiation, the antimicrobial effect is significantly improved at each concentration during the photothermal-magnetolytic coupling action. In summary, NiFe$_2$O$_4$@Au/PDA shows good photothermal bactericidal effects on both *E. coli* and *S. aureus* under near-infrared light irradiation, and with increasing concentration, the number of bacterial colonies decreases significantly. In addition, although the rotating magnetic field has limited antibacterial ability against bacteria, the effect of photothermal antibacterial will be substantially enhanced if the magnetic field is applied.

FESEM was applied to further study the antibacterial mechanism and observed a significant change in the morphology and membrane integrity of bacteria before and after treatment under different conditions. As shown in Fig. 9, *E. coli* and *S. aureus* have typical rod-like and spherical cell morphologies, with intact surfaces and regular shapes. Without using the photothermal material, the morphologies are not changed when only applying near-infrared light radiation (Fig. 9b, h). After co-
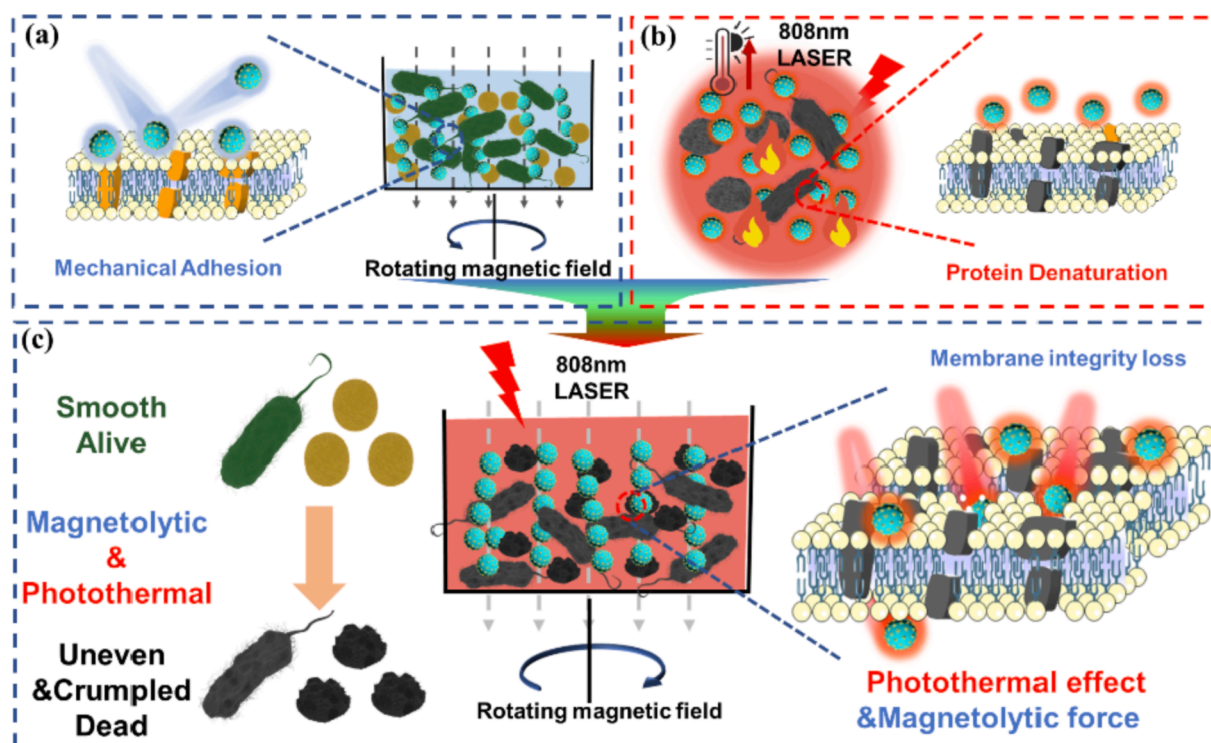
Fig. 10. Illustration of the interaction between particles and bacteria in the antibacterial process. Schematic diagram of antimicrobial activity under (a) magnetolytic condition, (b) photothermal condition and (c) photothermal- magnetolytic coupling condition.

culture with NiFe$_2$O$_4$@Au/PDA nanospheres, the intact rod (Fig. 9c) or spherical (Fig. 9i) cell morphologies can be well maintained without any treatment, indicating that the damage to bacteria by NiFe$_2$O$_4$@Au/PDA is negligible. When a rotating magnetic field is applied, the surfaces of some bacteria appear to be depressed, but the overall structure is relatively intact without obvious outflow of content, which indicates the magnetolytic effect is not obvious. As a comparison, when the NIR laser is conducted, significant crinkling and outflow of contents are observed in both *E. coli* and *S. aureus* in the presence of NiFe$_2$O$_4$@Au/PDA (Fig. 9e, k). Finally, when the photothermal-magnetolytic coupling process is applying, besides the shrinkage and rupture, significant deformation of the bacteria with pits appearing on the surface is clearly observed (Fig. 9f, l). As a result, the microscopic images characterization further support that the as-prepare NiFe$_2$O$_4$@Au/PDA nanospheres exhibit a wonderful photothermal-magnetolytic coupling anti-bacterial performance.

By combining the previous analysis and FESEM images, a schematic representation of the photothermal-magnetolytic coupling antibacterial process is proposed (Fig. 10). Under an external rotating magnetic field, the NiFe$_2$O$_4$@Au/PDA nanospheres are magnetized and the magnetic dipole–dipole interaction forces the nanospheres to form chain-like microstructures along the magnetic field (Fig. 10a). Due to the high stiffness of the cell wall, it is difficult for the rotating chain-like microstructure to exhibit direct magnetolytic effect. However, as has been reported in the literature [43,50,51], the interaction between the material and the bacteria increases due to the unique rough surface, resulting in some particles sticking to the cell wall. At the same time, combined with the equation of pressure, the rough surface has more bumps, resulting in a smaller area when acting. Therefore, compared to the smooth surface, the larger pressure can deliver from particles to bacteria under the action of the magnetic field, leading to a higher biodamage. When bacteria are exposed to near infrared light with the photothermal therapy reagent (NiFe$_2$O$_4$@Au/PDA), the reagent converts the light energy into heat. In general, bacteria cannot withstand such thermal effects because such high temperatures lead to
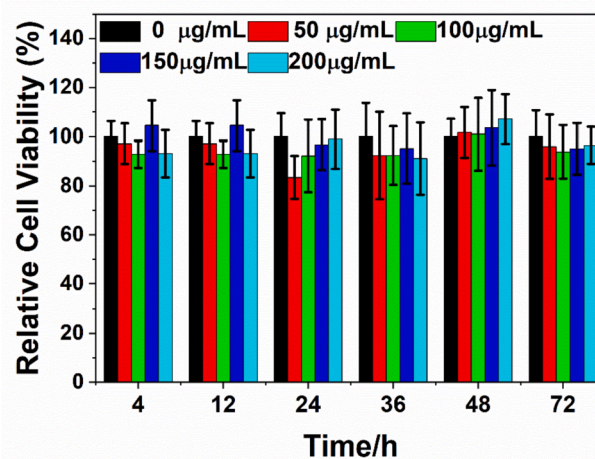

Fig. 11. Cell viability of REP1 cells treated by NiFe$_2$O$_4$@Au/PDA solutions with different concentrations and different time.

deformation of proteins and enzymes, induction of heat shock proteins, disruption of metabolic signals, etc. [52]. At this point, the selective permeability of the bacteria is disrupted, and the bacteria will crumple and the contents will flow out.

Eventually, the situation is quite different when the photothermal-magnetolytic coupling process is applied. In the first half of the action, as the temperature does not rise completely, the rotating magnetic field plays a leading role. In comparison to the pure photothermal treatment, the probability of contact between the particles and the bacteria is greater due to the rotating magnetic field. Moreover, it will be easier for rough surface particles to adhere to the surface of the bacteria in this case. This allows the hot particles to come into contact with the bacteria more quickly in the latter part of the antimicrobial process when the

temperature on the surface of the particles rises. This leads to a sharp decrease in the continuity of the bacterial surface, allowing particles impacting on the surface to penetrate into the bacteria and cause additional damage to the bacteria. Therefore, compared to the magnetic field alone, the magnetolytic effect begins to manifest and grows stronger with the gradual reduction of membrane integrity under photothermal conditions. So photothermal-magnetolytic coupling process provides a better antibacterial effect than either individual action.

Though the NiFe$_2$O$_4$@Au/PDA nanospheres presents a typical photothermal-magnetolytic coupling antibacterial performance, they are biocompatible due to the PDA surface, thus they possess high potential in many other bio-treatment areas. To verify the feasibility of *in vivo* application, the human retinal epithelial cells (REP1) were employed for cytotoxicity testing. Cell viability was assessed using the CCK-8 kit after co-culture of REP1 cells in different concentrations (0–200 μg/mL) of NiFe$_2$O$_4$@Au/PDA. As shown in Fig. 11, the samples exhibit high cell viability values and no significant increase in cytotoxicity with increasing dose. Cytotoxicity data also shows no significant decrease in cell activity even after co-culture for 72 h. This result must be mainly due to the good coating of PDA on the particle surface, which reduces cytotoxicity and allows the material to exhibit good biocompatibility. Due to the simple processing, remote conduction and low cytotoxicity, such interesting hypothetical applications may include, but are not limited to, antibacterial therapy, thrombolytic therapy, drug-targeted transport, and anticancer.

4. Conclusion

In this study, a rough surface NiFe$_2$O$_4$@Au/PDA core–shell nanosphere with excellent photothermal effect and unique magnetolytic effect has been developed *via* an *in situ* redox–oxidize polymerization. Due to the Au/PDA hybrid layer and the superparamagnetic NiFe$_2$O$_4$, the final product serves as a wonderful photothermal-magnetolytic coupling antibacterial agent. Furthermore, the mechanism of magnetolytic force is explored through rheological property measurements, chain model observations and molecular dynamics simulations. The experimental results show that the NiFe$_2$O$_4$@Au/PDA core–shell nanosphere possesses high photothermal sterilization effect (808 nm laser irradiation) against both Gram-positive and Gram-negative bacteria. The gradual appearance of the magnetolytic effect upon photothermal bactericidal suggests that magnetic photothermal antimicrobial reagents can be further enhanced by the action of a rotating magnetic field. An in-depth study of the photothermal-magnetolytic coupling antibacterial behavior is conducted by combining the experimental results and mechanism analysis. Cytotoxicity experiments have shown that the final product has a high biocompatibility. Therefore, besides antimicrobial therapy, this easily scalable magnetolytically enhanced photothermal effect is a great guide for other multifunctional magnetic photothermal nanoreagents in drug delivery, antitumor and thrombolysis, due to the simplicity of operation and the possibility of contact-free action.

Declaration of Competing Interest

The authors declare that they have no known competing financial interests or personal relationships that could have appeared to influence the work reported in this paper.

Acknowledgement

Appendix A. Supplementary data

Supplementary data to this article can be found online at https://doi.

org/10.1016/j.cej.2022.135282.

References

[1] A. Chatterjee, M. Modarai, N.R. Naylor, S.E. Boyd, R. Atun, J. Barlow, A.H. Holmes, A. Johnson, J.V. Robotham, Quantifying Drivers of Antibiotic Resistance in Humans: A Systematic Review, Lancet Infect. Dis. 18 (12) (2018) E368–E378, https://doi.org/10.1016/s1473-3099(18)30296-2.

[2] L. Xiao, Y.C. Guo, F. Wang, Y. Wang, X.S. Xu, W.Q. Ni, B.Y. Li, M.O. Xing, G.X. Luo, R.X. Zhan, A 3D Chemotactic-thermo-promo Bacterial Hunting System: Programmatic Bacterial Aattract, Capture, Killing and Healing the Wound, Chem. Eng. J. 417 (2021), https://doi.org/10.1016/j.cej.2020.128123.

[3] J.X. Liu, Tackling the Global Non-prescription Use of Antibiotics, Lancet Infect. Dis. 20 (2) (2020) 169–170, https://doi.org/10.1016/s1473-3099(19)30744-3.

[4] S. Meylan, I.W. Andrews, J.J. Collins, Targeting Antibiotic Tolerance, Pathogen by Pathogen, Cell 172 (6) (2018) 1228–1238, https://doi.org/10.1016/j.cell.2018.01.037.

[5] C. Cheng, S. Li, A. Thomas, N.A. Kotov, R. Haag, Functional Graphene Nanomaterials Based Architectures: Biointeractions, Fabrications, and Emerging Biological Applications, Chem. Rev. 117 (3) (2017) 1826–1914, https://doi.org/10.1021/acs.chemrev.6b00520.

[6] A. Bianchera, F. Buttini, R. Bettini, Micro/Nanosystems and Biomaterials for Controlled Delivery of Antimicrobial and Anti-biofilm Agents, Expert Opin. Ther. Patents 30 (12) (2020) 983–1000, https://doi.org/10.1080/13543776.2020.1839415.

[7] Y.Q. Wang, Y.Y. Jin, W. Chen, J.J. Wang, H. Chen, L. Sun, X. Li, J. Ji, Q. Yu, L.Y. Shen, B.L. Wang, Construction of Nanomaterials with Targeting Phototherapy Properties to Inhibit Resistant Bacteria and Biofilm Infections, Chem. Eng. J. 358 (2019) 74–90, https://doi.org/10.1016/j.cej.2018.10.002.

[8] P. Zhu, Y.u. Chen, J. Shi, Nanoenzyme-Augmented Cancer Sonodynamic Therapy by Catalytic Tumor Oxygenation, ACS Nano 12 (4) (2018) 3780–3795, https://doi.org/10.1021/acsnano.8b0099910.1021/acsnano.8b00999.s001.

[9] X. Zhuang, X. Ma, X. Xue, Q. Jiang, L. Song, L. Dai, C. Zhang, S. Jin, K. Yang, B. Ding, P.C. Wang, X.-J. Liang, A Photosensitizer-Loaded DNA Origami Nanosystem for Photodynamic Therapy, ACS Nano 10 (3) (2016) 3486–3495, https://doi.org/10.1021/acsnano.5b0767110.1021/acsnano.5b07671.s001.

[10] X.-D. Liu, B. Chen, G.-G. Wang, S. Ma, L.i. Cheng, W. Liu, L.i. Zhou, Q.-Q. Wang, Controlled Growth of Hierarchical Bi$_2$Se$_3$/CdSe-Au Nanorods with Optimized Photothermal Conversion and Demonstrations in Photothermal Therapy Adv, Funct. Mater. 31 (43) (2021) 2104424, https://doi.org/10.1002/adfm.202104424.

[11] Y. Liu, K. Ai, J. Liu, M.o. Deng, Y. He, L. Lu, Dopamine-Melanin Colloidal Nanospheres: An Efficient Near-Infrared Photothermal Therapeutic Agent for In Vivo Cancer Therapy, Adv. Mater. 25 (9) (2013) 1353–1359, https://doi.org/10.1002/adma.201204683.

[12] L.u. Li, X. Han, M. Wang, C. Li, T. Jia, X. Zhao, Recent Advances in the Development of Near-Infrared Organic Photothermal Agents, Chem. Eng. J. 417 (2021) 128844, https://doi.org/10.1016/j.cej.2021.128844.

[13] Y. Qian, D. Wang, X. Tian, H. Liu, X. Wang, H. Li, Q. Chen, X. Zhang, H. Wang, Synthesis of Urchin-like Nickel Nanoparticles with Enhanced Rotating Magnetic Field-Induced Cell necrosis and Tumor Inhibition, Chem. Eng. J. 400 (2020) 125823, https://doi.org/10.1016/j.cej.2020.125823.

[14] H. Chiriac, E. Radu, M. Tibu, G. Stoian, G. Ababei, L. Labusca, D.D. Herea, N. Lupu, Fe-Cr-Nb-B Ferromagnetic Particles with Shape Anisotropy for Cancer Cell Destruction by Magneto-mechanical Actuation, Sci Rep 8 (1) (2018) 11538, https://doi.org/10.1038/s41598-018-30034-3.

[15] A. Serrà, G. Vázquez-Mariño, J. García-Torres, M. Bosch, E. Vallés, Magnetic Actuation of Multifunctional Nanorobotic Platforms to Induce Cancer Cell Death, Adv. Biosyst. 2 (2) (2018) 1700220, https://doi.org/10.1002/adbi.201700220.

[16] N. Zhao, L. Yan, J. Xue, K. Zhang, F.-J. Xu, Degradable One-Dimensional Dextran-iron Oxide Nanohybrids for MRI-guided Synergistic Gene/photothermal/magnetolytic Therapy, Nano Today 38 (2021) 101118, https://doi.org/10.1016/j.nantod.2021.101118.

[17] Q.L. Fang, K.Z. Xu, Q.S. Xiong, Y.Q. Xu, A.L. Hui, S.H. Xuan, Fe$_3$O$_4$-Au-polydopamine Hybrid Microcapsules with Photothermal-photodynamic Synergistic Anti-bacterial Performance, CrystEngComm 23 (37) (2021) 6610–6619, https://doi.org/10.1039/d1ce00926e.

[18] W. Zeng, H. Zhang, Y. Deng, A. Jiang, X. Bao, M. Guo, Z. Li, M. Wu, X. Ji, X. Zeng, L. Mei, Dual-response Oxygen-generating MnO$_2$ Nanoparticles with Polydopamine Modification for Combined Photothermal-photodynamic Therapy, Chem. Eng. J. 389 (2020) 124494, https://doi.org/10.1016/j.cej.2020.124494.

[19] S. Zhang, Q. Lu, F. Wang, Z. Xiao, L. He, D. He, L.e. Deng, Gold-Platinum Nanodots with High-Peroxidase-like Activity and Photothermal Conversion Efficiency for Antibacterial Therapy, ACS Appl. Mater. Interfaces 13 (31) (2021) 37535–37544, https://doi.org/10.1021/acsami.1c0600010.1021/acsami.1c10600.s001.

[20] Y. Chen, Y.J. Gao, Y. Chen, L. Liu, A.C. Mo, Q. Peng, Nanomaterials-based Photothermal Therapy and Its Potentials in Antibacterial Treatment, J. Control. Release 328 (2020) 251–262, https://doi.org/10.1016/j.jconrel.2020.08.055.

[21] Z. Liu, X. Zhao, B. Yu, N. Zhao, C. Zhang, F.-J. Xu, Rough Carbon-Iron Oxide Nanohybrids for Near-Infrared-II Light-Responsive Synergistic Antibacterial Therapy, ACS Nano 15 (4) (2021) 7482–7490, https://doi.org/10.1021/acsnano.1c0089410.1021/acsnano.1c00894.s001.

[22] Y.Q. Qiao, X.M. Liu, B. Li, Y. Han, Y.F. Zheng, K.W.K. Yeung, C.Y. Li, Z.D. Cui, Y.Q. Liang, Z.Y. Li, S.L. Zhu, X.B. Wang, S.L. Wu, Treatment of MRSA-infected Osteomyelitis Using Bacterial Capturing, Magnetically Targeted Composites with

Microwave-assisted Bacterial Killing, Nat. Commun. 11 (1) (2020) 4446, https://doi.org/10.1038/s41467-020-18268-0.

[23] Q.S. Xiong, Q.L. Fang, K.Z. Xu, G.H. Liu, M. Sang, Y.Q. Xu, L.Y. Hao, S.H. Xuan, Near-infrared Light-responsive Photothermal α-Fe$_2$O$_3$@Au/PDA Core/shell Nanostructure with On-off Controllable Anti-bacterial Effects, Dalton Trans. 50 (40) (2021) 14235–14243, https://doi.org/10.1039/d1dt02251b.

[24] K. Yang, H. Xu, L. Cheng, C.Y. Sun, J. Wang, Z. Liu, In Vitro and In Vivo Near-Infrared Photothermal Therapy of Cancer Using Polypyrrole Organic Nanoparticles, Adv. Mater. 24 (41) (2012) 5586–5592, https://doi.org/10.1002/adma.201202625.

[25] Y. Zhao, T. Zhao, Y. Cao, J. Sun, Q. Zhou, H. Chen, S. Guo, Y. Wang, Y. Zhen, X.-J. Liang, S. Zhang, Temperature-Sensitive Lipid-Coated Carbon Nanotubes for Synergistic Photothermal Therapy and Gene Therapy, ACS Nano 15 (4) (2021) 6517–6529, https://doi.org/10.1021/acsnano.0c0879010.1021/acsnano.0c08790.s001.

[26] T.-T. Ngo-Duc, Z. Alibay, J.M. Plank, J.E. Cheeney, E.D. Haberer, Gold-Decorated M13 I-Forms and S-Forms for Targeted Photothermal Lysis of Bacteria, ACS Appl. Mater. Interfaces 12 (1) (2020) 126–134, https://doi.org/10.1021/acsami.9b1568210.1021/acsami.9b15682.s001.

[27] D. Liu, L. Ma, L. Liu, L.u. Wang, Y. Liu, Q.i. Jia, Q. Guo, G.e. Zhang, J. Zhou, Polydopamine-Encapsulated Fe$_3$O$_4$ with an Adsorbed HSP70 Inhibitor for Improved Photothermal Inactivation of Bacteria, ACS Appl. Mater. Interfaces 8 (37) (2016) 24455–24462, https://doi.org/10.1021/acsami.6b0811910.1021/acsami.6b08119.s001.

[28] Q. Gao, X. Zhang, W. Yin, D. Ma, C. Xie, L. Zheng, X. Dong, L. Mei, J. Yu, C. Wang, Z. Gu, Y. Zhao, Functionalized MoS$_2$ Nanovehicle with Near-Infrared Laser-Mediated Nitric Oxide Release and Photothermal Activities for Advanced Bacteria-Infected Wound Therapy, Small 14 (45) (2018) 1802290, https://doi.org/10.1002/smll.201802290.

[29] Z. Yu, L. Jiang, R. Liu, W. Zhao, Z. Yang, J. Zhang, S. Jin, Versatile Self-assembled MXene-Au Nanocomposites for SERS Detection of Bacteria, Antibacterial and Photothermal Sterilization, Chem. Eng. J. 426 (2021), 131914.

[30] Y. Cheng, S. Zhang, N. Kang, J. Huang, X. Lv, K. Wen, S. Ye, Z. Chen, X.i. Zhou, L. Ren, Polydopamine-Coated Manganese Carbonate Nanoparticles for Amplified Magnetic Resonance Imaging-Guided Photothermal Therapy, ACS Appl. Mater. Interfaces 9 (22) (2017) 19296–19306, https://doi.org/10.1021/acsami.7b0308710.1021/acsami.7b03087.s001.

[31] L.S. Lin, Z.X. Cong, J.B. Cao, K.M. Ke, Q.L. Peng, J.H. Gao, H.H. Yang, G. Liu, X. Y. Chen, Multifunctional Fe$_3$O$_4$@Polydopamine Core-Shell Nanocomposites for Intracellular mRNA Detection and Imaging-Guided Photothermal Therapy, ACS Nano 8 (4) (2014) 3876–3883, https://doi.org/10.1021/nn500722y.

[32] Q. Li, Y. Zhang, X. Huang, D. Yang, L. Weng, C. Ou, X. Song, X. Dong, An NIR-II Light Responsive Antibacterial Gelation for Repetitious Photothermal/thermodynamic Synergistic Therapy, Chem. Eng. J. 407 (2021) 127200, https://doi.org/10.1016/j.cej.2020.127200.

[33] X. Sun, L. Li, H. Zhang, M. Dong, J. Wang, P. Jia, T. Bu, X. Wang, L.i. Wang, Near-Infrared Light-Regulated Drug-Food Homologous Bioactive Molecules and Photothermal Collaborative Precise Antibacterial Therapy Nanoplatform with Controlled Release Property, Adv. Healthc. Mater. 10 (16) (2021) 2100546, https://doi.org/10.1002/adhm.202100546.

[34] X. Fan, F. Yang, C. Nie, L. Ma, C. Cheng, R. Haag, Biocatalytic Nanomaterials: A New Pathway for Bacterial Disinfection, Adv. Mater. 33 (33) (2021) 2100637, https://doi.org/10.1002/adma.202100637.

[35] S.K. Shaw, J. Kailashiya, A. Gangwar, S.K. Alla, S.K. Gupta, C.L. Prajapat, S. S. Meena, D. Dash, P. Maiti, N.K. Prasad, γ-Fe$_2$O$_3$ Nanoflowers as Efficient Magnetic Hyperthermia and Photothermal Agent, Appl. Surf. Sci. 560 (2021), 150025.

[36] Y.a. Li, Z. Qi, J. Yang, M. Zhou, X. Zhang, W. Ling, Y. Zhang, Z. Wu, H. Wang, B. Ning, H. Xu, W. Huo, X. Huang, Origami NdFeB Flexible Magnetic Membranes with Enhanced Magnetism and Programmable Sequences of Polarities, Adv. Funct. Mater. 29 (44) (2019) 1904977, https://doi.org/10.1002/adfm.201904977.

[37] Y.I. Golovin, A.O. Zhigachev, M.V. Efremova, A.G. Majouga, A.V. Kabanov, N. L. Klyachko, Ways and Methods for Controlling Biomolecular Structures Using Magnetic Nanoparticles Activated by an Alternating Magnetic Field, Nanotechnol. Russ. 13 (5–6) (2018) 295–304, https://doi.org/10.1134/s1995078018030072.

[38] Y.J. Shen, C.Y. Wu, T.Q.P. Uyeda, G.R. Plaza, B. Liu, Y. Han, M.S. Lesniak, Y. Zhang, Elongated Nanoparticle Aggregates in Cancer Cells for Mechanical Destruction with Low Frequency Rotating Magnetic Field, Theranostics 7 (6) (2017) 1735–1748, https://doi.org/10.7150/thno.18352.

[39] Y. Chen, P. Han, Y. Wu, Z. Zhang, Y. Yue, W. Li, M. Chu, Hedgehog-Like Gold-Coated Magnetic Microspheres that Strongly Inhibit Tumor Growth through Magnetomechanical Force and Photothermal Effects, Small 14 (45) (2018) 1802799, https://doi.org/10.1002/smll.201802799.

[40] S.-H. Hu, X. Gao, Nanocomposites with Spatially Separated Functionalities for Combined Imaging and Magnetolytic Therapy, J. Am. Chem. Soc. 132 (21) (2010) 7234–7237, https://doi.org/10.1021/ja102489q.

[41] M. Chen, J. Wu, P. Ning, J. Wang, Z. Ma, L. Huang, G.R. Plaza, Y. Shen, C. Xu, Y. u. Han, M.S. Lesniak, Z. Liu, Y.u. Cheng, Remote Control of Mechanical Forces via Mitochondrial-Targeted Magnetic Nanospinners for Efficient Cancer Treatment, Small 16 (3) (2020) 1905424, https://doi.org/10.1002/smll.201905424.

[42] A. Elbourne, S. Cheeseman, P. Atkin, N.P. Truong, N. Syed, A. Zavabeti, M. d. Mohiuddin, D. Esrafilzadeh, D. Cozzolino, C.F. McConville, M.D. Dickey, R. J. Crawford, K. Kalantar-Zadeh, J. Chapman, T. Daeneke, V.K. Truong, Antibacterial Liquid Metals: Biofilm Treatment via Magnetic Activation, ACS Nano 14 (1) (2020) 802–817, https://doi.org/10.1021/acsnano.9b0786110.1021/acsnano.9b07861.s001.

[43] Y. Dong, L.u. Wang, K.e. Yuan, F. Ji, J. Gao, Z. Zhang, X. Du, Y. Tian, Q. Wang, L. i. Zhang, Magnetic Microswarm Composed of Porous Nanocatalysts for Targeted Elimination of Biofilm Occlusion, ACS Nano 15 (3) (2021) 5056–5067, https://doi.org/10.1021/acsnano.0c1001010.1021/acsnano.0c10010.s00110.1021/acsnano.0c10010.s00210.1021/acsnano.0c10010.s00310.1021/acsnano.0c10010.s00410.1021/acsnano.0c10010.s00510.1021/acsnano.0c10010.s006.

[44] K. Xu, J. Wu, Q. Fang, L. Bai, J. Duan, J. Li, H. Xu, A. Hui, L. Hao, S. Xuan, Magnetically Separable h-Fe3O4@Au/polydopamine Nanosphere with a Hollow Interior: A versatile Candidate for Nanocatalysis and Metal Ion Adsorption, Chem. Eng. J. 398 (2020) 125571, https://doi.org/10.1016/j.cej.2020.125571.

[45] W. Cheng, K. Tang, Y. Qi, J. Sheng, Z. Liu, One-step synthesis of superparamagnetic monodisperse porous Fe$_3$O$_4$ hollow and core-shell spheres, J. Mater. Chem. 20 (9) (2010) 1799, https://doi.org/10.1039/b919164j.

[46] Q. Fang, J. Zhang, L. Bai, J. Duan, H. Xu, K. Cham-Fai Leung, S. Xuan, In Situ Redox-oxidation Polymerization for Magnetic Core-Shell Nanostructure with Polydopamine-encapsulated-Au hybrid Shell, J. Hazard. Mater. 367 (2019) 15–25, https://doi.org/10.1016/j.jhazmat.2018.12.059.

[47] H. Lee, S.M. Dellatore, W.M. Miller, P.B. Messersmith, Mussel-inspired Surface Chemistry for Multifunctional Coatings, Science 318 (5849) (2007) 426–430, https://doi.org/10.1126/science.1147241.

[48] L. Yan, J. Mu, P.X. Ma, Q. Li, P.X. Yin, X. Liu, Y.Y. Cai, H.P. Yu, J.C. Liu, G. Q. Wang, A.H. Liu, Gold Nanoplates with Superb Photothermal Efficiency and Peroxidase-like Activity for Rapid and Synergistic Antibacterial Therapy, Chemical Communications 57 (9) (2021) 1133–1136, https://doi.org/10.1039/d0cc06925f.

[49] A. Stukowski, Visualization and Analysis of Atomistic Simulation Data with OVITO-the Open Visualization Tool, Model. Simul. Mater. Sci. Eng. 18 (1) (2010) 015012, https://doi.org/10.1088/0965-0393/18/1/015012.

[50] F. Wei, X. Cui, Z. Wang, C. Dong, J. Li, X. Han, Recoverable Peroxidase-like Fe$_3$O$_4$@MoS$_2$-Ag Nanozyme with Enhanced Antibacterial Ability, Chem. Eng. J. 408 (2021), 127240.

[51] H. Song, Y. Ahmad Nor, M. Yu, Y. Yang, J. Zhang, H. Zhang, C. Xu, N. Mitter, C. Yu, Silica Nanopollens Enhance Adhesion for Long-Term Bacterial Inhibition, J. Am. Chem. Soc. 138 (20) (2016) 6455–6462.

[52] B. Rudolph, K.M. Gebendorfer, J. Buchner, J. Winter, Evolution of *Escherichia coli* for Growth at High Temperatures, J. Biol. Chem. 285 (25) (2010) 19029–19034.